# Urban Road Safety Prediction: A Satellite Navigation Perspective
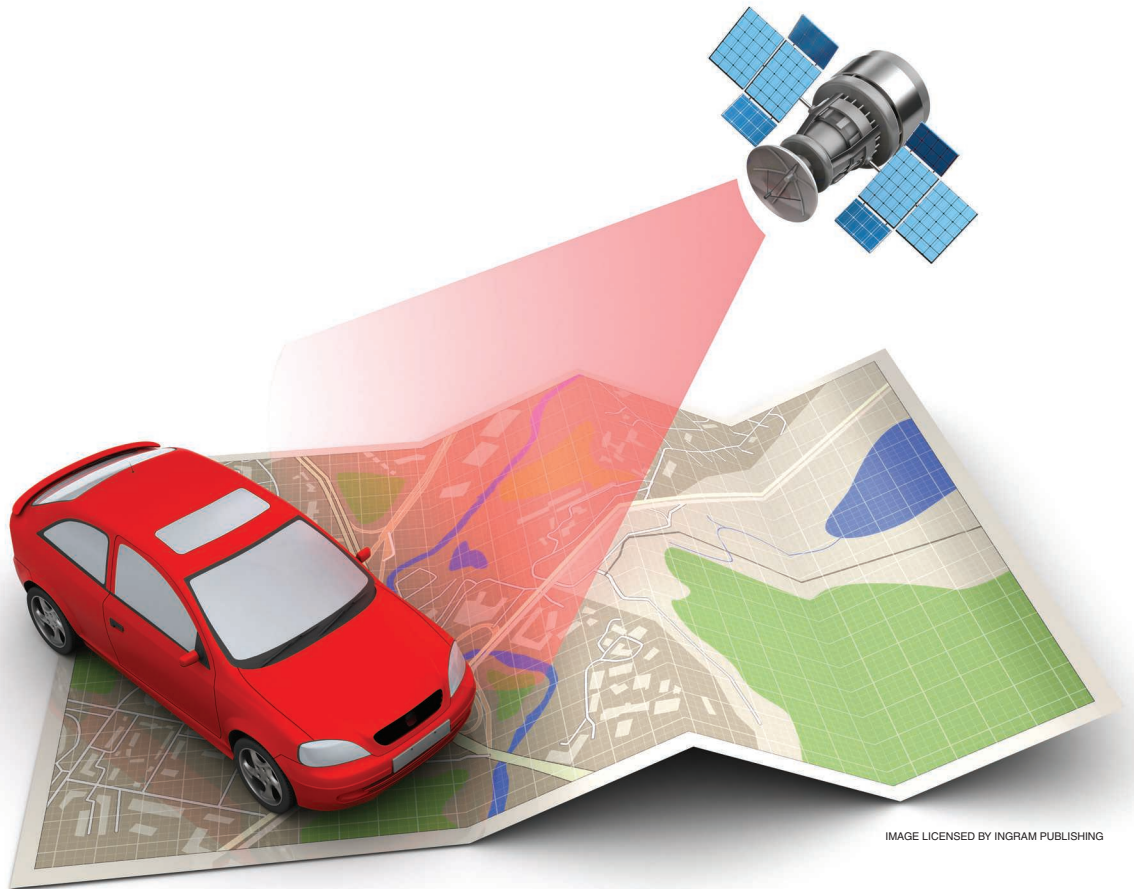


IMAGE LICENSED BY INGRAM PUBLISHING

**Halim Lee** and **Jiwon Seo** *
*Are with Yonsei University, Incheon, 21983, Korea.*
*E-mail: halim.lee@yonsei.ac.kr; jiwon.seo@yonsei.ac.kr*

**Zaher M. Kassas** *
*Is with The Ohio State University, Columbus, Ohio, 43210, USA.*
*E-mail: zkassas@ieee.org*

*Corresponding authors

*Abstract*—Predicting the safety of urban roads for navigation via global navigation satellite systems (GNSS) signals is considered. To ensure the safe driving of automated vehicles, a vehicle must plan its trajectory to avoid navigating on unsafe roads (e.g., icy conditions, construction zones, narrow streets, and so on). Such information can be derived from roads' physical properties, the vehicle's capabilities, and weather conditions. From a GNSS-based navigation perspective, the reliability of GNSS signals in different locales, which is heavily dependent on the road layout within the surrounding environment, is crucial to ensure safe automated driving. An urban road environment surrounded by tall objects can significantly degrade the accuracy and availability of GNSS signals. This article proposes an approach to predict the reliability of GNSS-based navigation to ensure safe urban navigation. Satellite navigation reliability at a given location and time on a road is determined based on the probabilistic position error bound of the vehicle-mounted GNSS receiver. A metric for GNSS reliability for ground vehicles is suggested, and a method to predict the conservative probabilistic error bound of the GNSS navigation solution is proposed. A satellite navigation reliability map is generated for various navigation applications. As a case study, the reliability map is used in a proposed optimization problem formulation for automated ground vehicle safety-constrained path planning.

For the safe and reliable control of automated ground vehicles, various road information needs to be estimated. Road information typically include road surface conditions, such as dryness, wetness, and iciness, as well as shapes, including curvature, bank angles, and slope angles. Satellite-based navigation reliability should also be considered important road information because automated vehicles use various navigation sensors that are dependent on positioning, navigation, and timing from global navigation satellite systems (GNSS). In particular, reliable and accurate GNSS-derived positions are crucial for short-range driving control and long-range navigation and path planning, while timing is crucial for onboard sensor fusion, cooperative planning and control, and information exchanges with other vehicles and the infrastructure. The reliability and accuracy of received GNSS signals is heavily dependent on the road layout within the surrounding environment.

An automated vehicle usually relies on GNSS, such as GPS in the United States, GLONASS in Russia, Galileo in Europe, and Beidou in China, to obtain its absolute position on Earth. Although other sensors, including vision [1], [2], radar [3], [4], lidar [5], [6], and ultrasonic [7] sensors and sensor networks [8], [9], can measure relative distances to nearby objects, GNSS receivers are the primary sensing modality for determining a vehicle's absolute position. This absolute position information is crucial, especially for initializing urban navigation processes using other sensors. For example, given a GNSS position solution, one can narrow the search space in digital maps, which are used with 3D point clouds from a scanning lidar, to estimate in real time a vehicle's position and heading to lane-level accuracy to avoid collisions [10]. In addition, when integrated with vision simultaneous localization and mapping [2], GNSS can mitigate the accumula-tive positioning error. Furthermore, GNSS measurements can be used to fix the drift of inertial measurement units (IMUs) for determining a vehicle's linear and angular motion [11], [12].

GNSS and differential correction stations alone can provide centimeter-level positioning accuracy if the signal reception environment and solar activity are favorable [17]. Urban canyons impose harsh signal reception conditions [18]. Tall buildings, trees, and nearby vehicles frequently block GNSS signals. Non-line-of-sight (NLOS) reception of GNSS signals without the reception of LOS signals, i.e., the NLOS-only condition, which occasionally occurs on urban roads, can cause arbitrarily large position errors. In addition, the accuracy of pseudoranges (i.e., measured distances between a user's receiver and GNSS satellites, without compensating for the receiver's clock bias and atmospheric delays) is degraded in an urban environment where LOS and NLOS signals are simultaneously received, i.e., the LOS + NLOS condition. Therefore, it is important to predict the reliability of GNSS signals on urban roads to ensure the safe operation of automated ground vehicles.

Various studies have utilized 3D building models with and without ray tracing to overcome the unfavorable GNSS signal reception conditions in urban environments [13], [14], [19]–[21]. Power matching [22], shadow matching [20], specular matching [21], and urban trench modeling [19] were developed to decrease positioning error by predicting the NLOS conditions of GNSS satellites by using a 3D building map. In [13] and [14], 3D building models along with ray-tracing techniques were utilized to predict pseudoranges at a given location in an urban multipath environment. The future state uncertainty [13] and predicted positioning error [14] were then calculated based on the predicted pseudoranges. However, while GNSS signal blockage due to buildings was considered, blockage due to other objects

(e.g., trees and nearby vehicles) was not considered, nor did the predicted positioning error consider the detection and exclusion of possible faulty satellite signals and the probabilistic error bound of the predicted position solution.

The probabilistic error bound of the GNSS position solution, which is referred to as the *protection level* (*PL*), as well as the concept of navigation integrity have been actively studied for safety-critical applications, such as aviation [23], [24]. In [15], a receiver autonomous integrity monitoring (RAIM) algorithm was developed to predict the horizontal position error bound [i.e., the horizontal PL (HPL)] as a measure of satellite navigation reliability for ground vehicles. However, this algorithm did not perform fault detection and exclusion (FDE), and it did not consider multiple signal faults, which are expected in urban environments. Furthermore, urban NLOS-only and LOS + NLOS conditions were not considered, and it was assumed that all GPS signals were received by direct LOS.

To overcome these limitations, a multiple hypothesis solution separation (MHSS) RAIM method was applied in [16], which considered multiple signal faults to predict the HPL. However, FDE was still not performed, and the performance of the proposed method was not validated experimentally. Upon attempting to validate this method experimentally, it was discovered that the method did not accurately predict the HPL. This was due to the complexity of predicting the multipath environment sufficiently accurately and due to signal blockage owing to tall objects other than buildings. As presented in Table 1, the method proposed in the current study addresses the aforementioned issues.

The contributions of this study are summarized as follows:

- A conservatively predicted multiconstellation GNSS HPL, after detecting and excluding multiple signal faults, is suggested as a metric for GNSS reliability for ground vehicles. This metric considers more realistic urban GNSS signal environments than those in Table 1.

- A method to conservatively predict GNSS HPLs for ground vehicles is proposed. While performing ray-tracing simulations with 3D urban digital maps, possible driving lanes and surrounding vehicles are considered, and the most conservative value is selected at each longitudinal location along the test roads.

- It is experimentally shown that the proposed metric (i.e., the conservatively predicted HPL) successfully overbounds the HPL calculated using real pseudorange measurements during field tests in two cities.

- An optimization problem formulation for safety-constrained path planning is proposed. Unlike previous studies, the unavailability of GNSS signals and continuous GNSS signal outages are considered in the problem formulation. A specific implementation to solve this problem is also presented and experimentally demonstrated. The proposed method enables automated ground vehicles to select the path that ensures navigation safety.

## Prediction of Satellite Navigation Reliability on Urban Roads

A GNSS receiver estimates its 3D position and clock bias by using pseudorange measurements from at least four GNSS satellites. Because a pseudorange is directly related to the signal travel time from a satellite to a user's receiver, which is measured by a receiver clock, various errors, such as satellite clock bias and ionospheric and tropospheric delay errors, contaminate the pseudorange measurement. These errors should be corrected for to bring the pseudorange closer to the true range. The receiver clock bias is treated as an additional unknown variable, which is obtained alongside the receiver position through a solution estimation process. This section presents various error sources for satellite navigation systems and introduces the proposed method to predict pseudoranges and conservative position error

| Method | Metric for GNSS Reliability | Considered Obstacles | Verification Method |
|---|---|---|---|
| Shetty and Gao [13] | State uncertainty bound ($3\sigma$) that encloses the uncertain future state distributions | Buildings in virtual urban environments | Simulations only |
| Zhang and Hsu [14] | GPS positioning error | Real-world buildings, without consideration of driving lanes | Experiments (mean of the measured and predicted positioning errors differed by a maximum of 17.7 m) |
| Maaref and Kassas [15] | GPS HPL without consideration of measurement faults | Not considered (all GPS signals assumed to be direct LOS) | Experiments (no performance comparison between the predicted and measured HPLs reported) |
| Lee et al. [16] | GPS HPL with consideration of multiple measurement faults (FDE not performed) | Real-world buildings, without consideration of driving lanes | Simulations only |
| Proposed | Conservative multiconstellation GNSS HPL with consideration of multiple measurement faults (FDE performed) | Real-world buildings and surrounding vehicles, with consideration of driving lanes | Experiments (conservatively predicted HPL bounded the measured HPL 100% of the time) |

Table 1. The comparison of GNSS reliability prediction methods.

bounds as measures of satellite navigation reliability on urban roads.

## Error Sources for Satellite Navigation

The performance of GNSS-based navigation can be degraded by anomalous ionospheric behavior [25]–[27], radio frequency interference [28], [29], signal reflection and blockage [30], [31], and poor geometric diversity of satellites in view [32], [33]. In particular, signal reflection and blockage due to buildings and other tall objects is a significant error source for ground vehicle navigation in urban canyons. When $N$ GNSS satellites are in view, the $n$th pseudorange measurement in an urban environment at time step $t$, after satellite clock bias corrections, can be modeled as follows:

$$
\begin{aligned}
\rho^n(t) &= R_{\text{LOS}}^n(t) + \rho_{\text{bias}}^n(t) + \varepsilon^n(t) \\
&= \| \boldsymbol{r}_u(t) - \boldsymbol{r}^n(t) \|_2 + c \cdot \delta t_u(t) \\
&\quad + I^n(t) + T^n(t) + \rho_{\text{bias}}^n(t) + \varepsilon^n(t),
\end{aligned}
\tag{1}
$$

where the descriptions of the symbols are given in Table 2.

Considerable common-mode errors can exist between a user and a nearby reference station, such as atmospheric delays and satellite ephemeris errors. These errors can be largely mitigated using differential GNSS (DGNSS). A DGNSS reference station broadcasts correction messages to nearby users, enabling the users to eliminate common-mode errors. However, site-specific errors caused by NLOS-only and LOS + NLOS signal reception cannot be mitigated using DGNSS.

Four GNSS signal reception conditions can occur in urban canyons: 1) the LOS-only condition, in which only the LOS signal is received; 2) the NLOS-only condition, in which only NLOS signals are received; 3) the LOS + NLOS condition, in which both LOS and NLOS signals are received; and 4) the no-signal condition, in which a signal is completely blocked by an object. Figure 1 illustrates the difference between the NLOS-only and LOS + NLOS conditions. In the field of satellite navigation, the NLOS-only and LOS + NLOS conditions are treated differently, as they cause different types of pseudorange errors. Moreover, simulation methods to predict these errors are different, as discussed in the following.

Under the NLOS-only condition, the NLOS-only bias term, which is $\rho_{\text{NLOS}}^n$ in Figure 1(a), reflects the extra travel distance (i.e., $\rho_1^n - R_{\text{NLOS}}^n$ where $\rho_1^n$ is the travel distance along the reflected path) due to signal reflection, which

### Table 2. The mathematical notations related to pseudorange measurement modeling in urban environments.

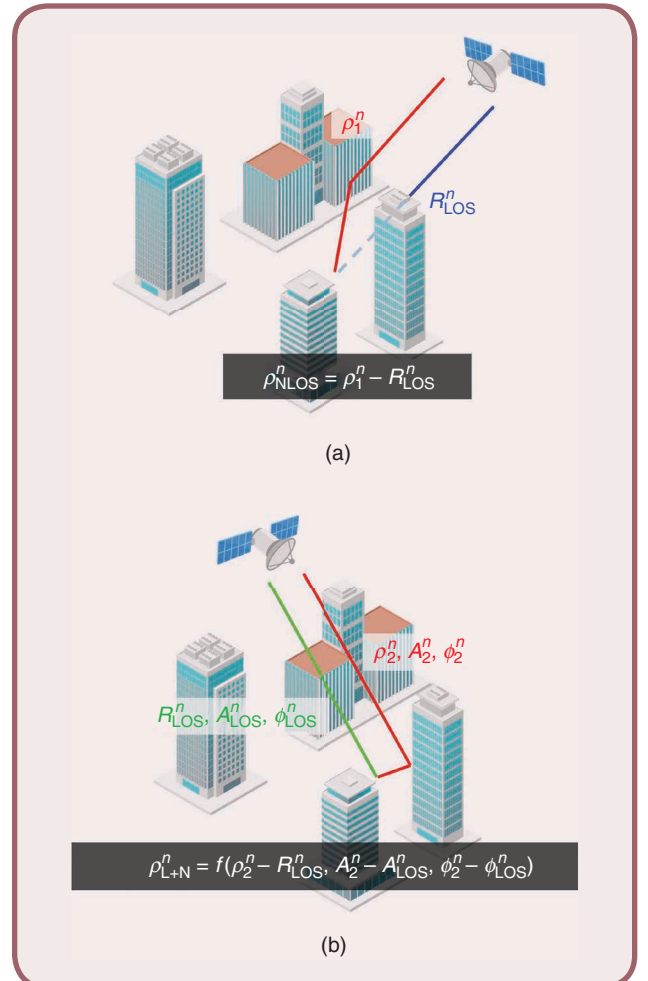| Symbol | Description |
|---|---|
| $\rho^n$ | The $n$th pseudorange measurement in an urban environment after satellite clock bias corrections |
| $R_{\text{LOS}}^n$ | Length of the LOS path between a user's receiver and the $n$th satellite, including delays due to receiver's clock bias, ionosphere, and troposphere |
| $\rho_{\text{bias}}^n$ | Either 1) the bias due to an NLOS-only condition (i.e., $\rho_{\text{NLOS}}^n$) which represents the extra travel distance of the NLOS signal compared with $R_{\text{LOS}}^n$ [see Figure 1(a)], or 2) the bias due to an LOS + NLOS condition (i.e., $\rho_{\text{L+N}}^n$) where both LOS and NLOS signals are received [see Figure 1(b)] |
| $\rho_{\text{NLOS}}^n$ | Bias due to an NLOS-only condition |
| $\rho_{\text{L+N}}^n$ | Bias due to an LOS + NLOS condition |
| $\boldsymbol{r}_u$ | Position vector of a user's receiver |
| $\boldsymbol{r}^n$ | Position vector of the $n$th satellite |
| $c$ | Speed of light |
| $\delta t_u$ | User's receiver clock bias |
| $I^n$ | Ionospheric delay in the $n$th pseudorange measurement |
| $T^n$ | Tropospheric delay in the $n$th pseudorange measurement |
| $\varepsilon^n$ | Remaining errors (e.g., noise, unmodeled effects, and so on) in the $n$th pseudorange measurement |



**FIG 1** The GNSS (a) NLOS-only and (b) LOS + NLOS conditions in an urban environment and corresponding pseudorange biases.

can be arbitrarily large. If this bias remains in the pseudorange measurement, it can cause a large unbounded positioning error. A typical way to predict $\rho_{\text{NLOS}}^n$ at a given location is to calculate the difference between the lengths of the direct and reflected paths (i.e., the LOS and NLOS paths) from a satellite to a receiver, which represents the extra travel distance. Ray-tracing simulation using 3D urban digital maps can be performed to estimate the length of the reflected path. The positions of the satellites at a given time for ray-tracing simulation are calculated based on the satellite broadcast almanac information. The complete blockage of a signal (i.e., the no-signal condition) can also be predicted by ray-tracing simulation.

In an urban environment, the LOS + NLOS condition is more frequently observed than the NLOS-only condition. Unlike the NLOS-only bias term, the LOS + NLOS bias term, which is $\rho_{\text{L+N}}^n$ in Figure 1, is bounded. Reflected signals with a large delay when compared with the 1.5-chip width of the GNSS signal (e.g., a 300-m width for a GPS L1 C/A-code chip) do not cause any bias in the pseudorange measurements if the direct signal is also received and tracked [34]. For short-delay reflected signals (i.e., the delay is less than 1.5 chips), $\rho_{\text{L+N}}^n$ depends on the receiver's correlator design, and it is a function of the difference of the travel distances (i.e., $\rho_2^n - R_{\text{LOS}}^n$), received signal amplitudes (i.e., $A_2^n - A_{\text{LOS}}^n$), and phases (i.e., $\phi_2^n - \phi_{\text{LOS}}^n$) of the reflected and direct signals, where $(\cdot)_2^n$ and $(\cdot)_{\text{LOS}}^n$ represent the reflected and direct signals from the $n$th satellite, respectively [see Figure 1(b)].

The receiver used in the field experiments of this study, which will be explained in the "Experimental Field Test Results" section, utilizes the a posteriori multipath estimation (APME) method [35]; therefore, the multipath error envelop of the APME method was used to predict $\rho_{\text{L+N}}^n$ in this study. The amplitudes and phases of the received reflected and direct signals were obtained through ray-tracing simulations.

### Probabilistic Error Bound and Advanced RAIM

Accuracy in the field of navigation usually refers to the 95th-percentile value of the positioning error distribution [36]. However, when navigation safety is of concern, a considerably higher probability (e.g., 99.99999% for the vertical guidance of aircraft) should be considered to obtain an error bound [23]. This error bound (i.e., the PL) includes the true position of a user with a required high probability. If the PL is larger than the alert limit (AL) of a certain safety-critical operation (e.g., 35 m for the vertical guidance of an aircraft down to 200 ft above the runway), the position output from the navigation system is deemed unreliable because it is not guaranteed that the true position is within the AL with the required probability. In this case, the navigation system is declared unavailable and must not be used to ensure navigation safety (i.e., navigation integrity is guaranteed by a timely alert).

Among various methods and augmentation systems—e.g., ground-based augmentation systems [37]–[39] and satellite-based augmentation systems [40], [41]—to guarantee the integrity of satellite navigation systems, RAIM is often preferred because it requires no or minimal support from infrastructure. The basic idea of RAIM is to check the consistency among position solutions obtained by subsets of pseudorange measurements. If all the subset solutions are almost identical, all the signals can be confirmed to be fault free, and the position output of a receiver is deemed reliable.

Many RAIM algorithms have the functionality of FDE and PL calculations. FDE rejects faulty signals that cause erroneous position solutions through a consistency check using redundant measurements. A minimum of six pseudorange measurements is necessary to detect and exclude a single fault. PL is a probabilistic error bound of a position solution, and HPL is particularly relevant to ground vehicles. For aerial vehicles, the vertical PL should also be considered [42], [43]. After performing FDE, the HPL can be calculated, as shown in Figure 2.

It should be noted that RAIM is suitable for the real-time integrity monitoring of received GNSS signals; however, the focus of this study is not on guaranteeing real-time navigation integrity. Instead, a method is proposed to predict satellite navigation reliability at every location on urban roads before an automated vehicle arrives at a location. The probabilistic position error bound (i.e., the HPL) is used as a safety metric to represent satellite navigation reliability. After the reliability is predicted and provided to a vehicle as part of the road information, the vehicle can detour around the low-reliability region (i.e., the high-HPL region) or prepare
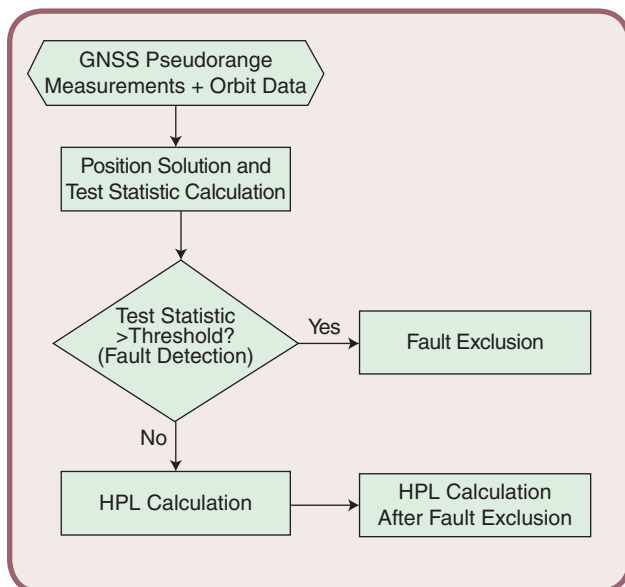


**FIG 2** The FDE and HPL calculation of the RAIM algorithm.

its other navigation sensors to not utilize GNSS measurements when passing through the low-reliability region.

For this purpose, advanced RAIM (ARAIM) with an MHSS algorithm [36], [44] that can handle multiple faults and constellations is adopted in this study. It is expected that a ground vehicle will experience multiple GNSS signal faults on urban roads. Currently, most GNSS receivers used by automated vehicles are capable of tracking multiple GNSS constellations (e.g., GPS and GLONASS were used in this study). By introducing multiple hypotheses of signal failures, ARAIM can detect and exclude multiple faults in multiple constellations and consider the possibility of further fault modes when calculating the HPL. Therefore, ARAIM, among various RAIM algorithms [45], is appropriate for FDE based on predicted pseudoranges and HPL prediction for automated ground vehicles in urban environments.

The MHSS-based FDE algorithm detects faulty signals by using a solution separation threshold test. Solution separation is the difference between fault-free and fault-tolerant position solutions. The receiver's state $x$, which is $\hat{x} + \Delta\hat{x}$, can be estimated by the weighted least-squares estimator, whose update equation is given by [34], [44]

$$\Delta\hat{x} = (\mathbf{G}^\top \mathbf{W} \mathbf{G})^{-1} \mathbf{G}^\top \mathbf{W} \Delta\boldsymbol{\rho}, \tag{2}$$

where the descriptions of the symbols are given in Table 3. The fault-free position solution is estimated from the all-in-view satellites, whereas the fault-tolerant position solution assumes one or more possible faulty signals; thus, it is estimated from a subset of satellites. Then, the solution separation threshold test is expressed as [44]

$$|\hat{x}_q^{(0)} - \hat{x}_q^{(k)}| \le T_{k,q}, \tag{3}$$

where the descriptions of the symbols are given in Table 3. If the solution separation for any axis exceeds a certain threshold, signal faults are likely to exist, and exclusion of these faults should be attempted.

If the solution separation threshold test passes without excluding any satellite signals, the HPL is computed as follows. In the MHSS-based HPL calculation method, the HPL is obtained as a bound that includes all the HPLs corresponding to the fault-free and fault-tolerant position solutions. The HPL for the $q$-axis (i.e., $HPL_q$) is calculated as [44]

| Symbol | Description |
|---|---|
| **x** | State vector of a user's receiver, which is defined as $[\mathbf{r}_u^\top, c\delta t_u]^\top$ |
| **ρ** | Pseudorange measurement vector, which is defined as $[\rho^1, \ldots, \rho^N]^\top$ |
| $\Delta\hat{x}$ | Difference between a receiver's state vector **x** and its estimate from the previous iteration $\hat{x}$ |
| $\Delta\boldsymbol{\rho}$ | Difference between the pseudorange measurement vector **ρ** and the expected pseudorange vector $\hat{\boldsymbol{\rho}}$ based on the satellite positions and $\hat{x}$ |
| **G** | Geometry matrix |
| **W** | Weighting matrix, which is the inverse of a diagonal matrix whose diagonal elements are the measurement noise variances |
| $q$ | Either $q = 1$ or $q = 2$ for the east or north axis of the horizontal plane, respectively |
| $\hat{x}_q^{(0)}$ | Fault-free position solution for the $q$-axis estimated from the all-in-view satellites |
| $\hat{x}_q^{(k)}$ | Fault-tolerant position solution for the $q$-axis and $k$th fault mode |
| $T_{k,q}$ | Solution separation threshold for the $q$-axis and $k$th fault mode ($k = 0$ represents the fault-free condition) |
| $HPL_q$ | HPL for the $q$-axis |
| $\mathbf{Q}(\cdot)$ | Tail probability function of the standard Gaussian distribution |
| $b_q^{(k)}$ | Nominal bias of the position solution for the $q$-axis and $k$th fault mode |
| $\sigma_q^{(k)}$ | Standard deviation of the position solution for the $q$-axis and $k$th fault mode |
| $N_{\text{fault modes}}$ | Total number of fault modes |
| $p_{\text{fault},k}$ | Probability that the $k$th fault mode occurs |
| $PHMI_{\text{HOR}}$ | Probability of hazardously misleading information for the horizontal component |
| $PHMI_{\text{VERT}}$ | Probability of hazardously misleading information for the vertical component |
| $P_{\text{sat,not monitored}}$ | Probability that independent simultaneous satellite faults are not monitored |
| $P_{\text{const,not monitored}}$ | Probability that simultaneous constellation faults are not monitored |

Table 3. The mathematical notations related to HPL calculation.

$$2\mathbf{Q}\left(\frac{HPL_q - b_q^{(0)}}{\sigma_q^{(0)}}\right)$$
$$+ \sum_{k=1}^{N_{\text{fault modes}}} p_{\text{fault},k} \mathbf{Q}\left(\frac{HPL_q - T_{k,q} - b_q^{(k)}}{\sigma_q^{(k)}}\right)$$
$$= \frac{1}{2}PHMI_{\text{HOR}}\left(1 - \frac{P_{\text{sat,not monitored}} + P_{\text{const,not monitored}}}{PHMI_{\text{VERT}} + PHMI_{\text{HOR}}}\right), \quad (4)$$

where the descriptions of the symbols are given in Table 3. Detailed information and mathematical formulations of the ARAIM user algorithm are provided in [44]. If the solution separation threshold test does not pass (i.e., a fault is detected), fault exclusion should be attempted. After the exclusion of faulty signals, the HPL should be calculated considering the probability of wrong exclusion. The HPL equation in this case has an additional factor to (4). Detailed discussions are available in [44].

*Prediction of Conservative HPL in Urban Environments*
Predicting the exact HPL of a vehicle at a certain location and time is virtually impossible due to imperfections in
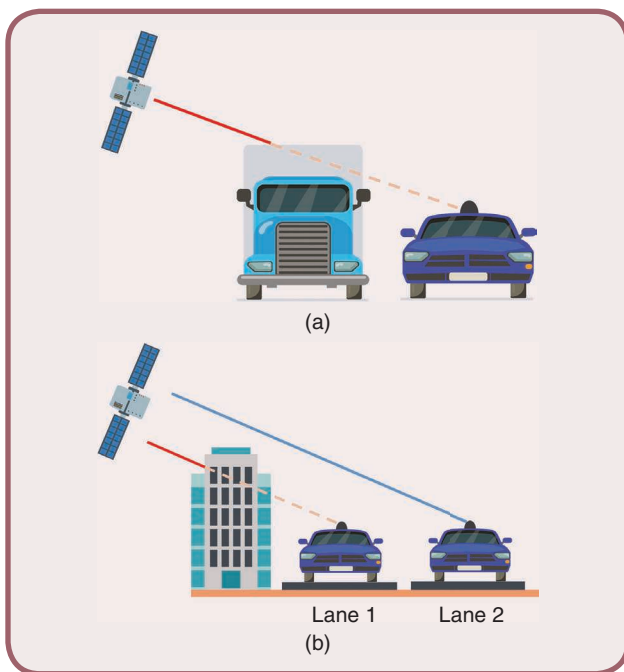


**FIG 3** (a) The GNSS signal blockage due to a nearby vehicle. (b) The different signal reception conditions in two lanes.
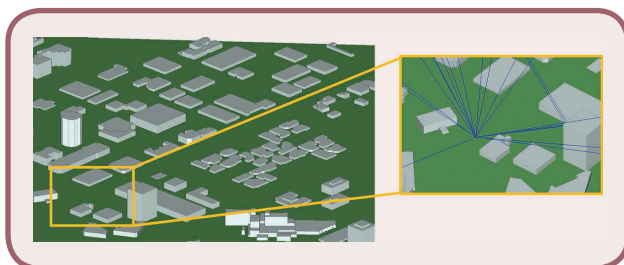


**FIG 4** The ray tracing at a single node within a 3D urban digital map.

3D urban digital maps as well as the presence of nearby dynamic objects, which cannot be predicted. For example, nearby vehicles can block satellite signals, as illustrated in Figure 3(a). Therefore, the HPL will be predicted conservatively by assuming that the vehicle of interest is always surrounded by taller vehicles. Considering the height of the vehicle used for the field test (1.7 m), the height and width of a typical dump truck (3.3 and 2.5 m, respectively), and the typical width of a lane (3.7 m), an elevation mask of 33° was set, including a slight margin. In other words, to be conservative, satellite signals with less than a 33° elevation are assumed to be blocked by nearby vehicles.

Signal reflection and blockage due to static objects, such as buildings, can be predicted by ray-tracing simulation if exact 3D urban digital maps are available [46], [47]. However, it should be noted that the signal reception conditions in each lane can vary significantly [48]. For example, a vehicle can have an LOS reception of a certain satellite signal in one lane but may not receive the signal from the same satellite in another lane because of building blockage [see Figure 3(b)].

To perform ray-tracing simulations to predict signal blockage due to buildings and NLOS-only or LOS + NLOS bias (i.e., $\rho_{\text{NLOS}}^n$ or $\rho_{\text{L+N}}^n$ in Figure 1), commercial 3D urban digital maps from 3dbuildings and Wireless InSite commercial ray-tracing software were used. Figure 4 shows an example of a ray-tracing simulation. It was assumed that the exterior walls of all buildings were made of concrete. The time of arrival (TOA) of GNSS signals was calculated using the shooting and bouncing ray (SBR) method described in [49], which is used to find geometrical propagation paths between a transmitter and a receiver using a 3D map. In the SBR method, among the rays transmitted from the source, the rays that hit the building are specularly reflected and traced until the maximum number of reflections is reached. Then, $\rho_{\text{NLOS}}^n$ or $\rho_{\text{L+N}}^n$ is predicted using the simulated TOAs, amplitudes, and phases of GNSS signals from ray tracing according to the signal reception condition. The GPS and GLONASS constellations were considered based on their almanac information.

To reduce the computational complexity of the ray-tracing simulation, it was assumed that the receiver received only direct and single reflected signals. If a signal was reflected by buildings more than once, it was assumed that the signal was not received by the vehicle. This assumption does not significantly affect the accuracy of conservative HPL prediction because the received signal strength of multiple reflected signals is low, and a receiver may not track such signals.

With the predicted pseudoranges from the ray-tracing simulation, the HPL can be predicted following the procedure in Figure 2. An example map of the conservatively predicted HPL is given in Figure 5. If the number of visible satellites at a certain location is insufficient for FDE, the location is marked as unavailable because the HPL prediction is not performed in this case. It should be noted that the HPL

at a given location varies with time because GNSS satellites move. Fortunately, future satellite positions are reliably predictable based on ephemerides [34]. Thus, the conservative HPLs over a certain time horizon at each location can be calculated in advance in a cloud server. Automated vehicles can use this information without concern about their onboard computational power. Since the conservative HPL prediction at each location and time can be performed independently, a cloud server with enough parallel processors can quickly generate HPL prediction maps of regions of interest.

### Experimental Field Test Results

To verify the proposed methodology for conservatively predicting HPL in urban environments, field tests were performed to calculate the HPL based on actual pseudorange measurements. Then, the HPL based on measured pseudoranges (i.e., the measured HPL) was compared with the conservative HPL based on predicted pseudoranges (i.e., the conservatively predicted HPL). The HPL varies over time, as satellite geometry changes. Further, the HPL is impacted by the surrounding environment. To check if the proposed methodology is applicable to various times and environments, field tests were performed in two different cities: Irvine, California, and Riverside, California.

During the experiments, GPS and GLONASS measurements were collected using a Septentrio AsteRx-i V receiver. The GNSS antenna was placed on top of the ground vehicle (Figure 6). GNSS constellations during the experiments in Irvine and Riverside are included in Figure 7. Figure 8 presents a small portion of the urban test environment in Irvine as an example, which included several tall buildings that significantly changed the measured HPL values. In Riverside, complex-shaped buildings were distributed along the test trajectory. The experiments were conducted along approximately 4.5- and 1.6-km roads in Irvine and Riverside, respectively.

As shown in Figure 3(b), the signal reception condition can dramatically change according to the lateral location of a vehicle on the road. It is theoretically possible to predict the HPL at every location, as in Figure 5; however, the prediction accuracy depends on the accuracy of the 3D building and road maps. For example, a slight height error of a building model or a lateral position error of a road model in a digital map can cause a visible satellite to be predicted as invisible during ray-tracing simulation. Unfortunately, commercially available 3D digital maps have limited accuracy. As a conservative approach, multiple ray-tracing simulations were performed by changing the vehicle's lateral location across the road. If a certain satellite was invisible at one location, the satellite was treated as an invisible satellite when predicting the HPL at the given longitudinal location of the road. Furthermore, $\rho_{NLOS}^n$ and $\rho_{L+N}^n$ were also predicted at every lateral location across the road, and the largest value was chosen for the pseudorange prediction, to be conservative.

Figure 9 describes the conservatively predicted HPL along two 1.5-km roads with tall buildings. The ground vehicle freely changed its driving lane during the field tests. However, its measured HPL was always less than the conservatively predicted HPL that assumed the most challenging lateral location, having the largest number of signal blockages and largest NLOS-only and LOS + NLOS biases. When the vehicle drove along a lane with better satellite visibility (i.e., a lane distant from a tall building), the measured HPL was significantly lower than the conservatively predicted HPL that assumed the most challenging lane with poor satellite visibility, as in the case of a 1.3-km distance location in Figure 9(b). Nevertheless, the most challenging lane needs to be assumed when the HPL is predicted because it is not practical to restrict the driving lane of a vehicle.
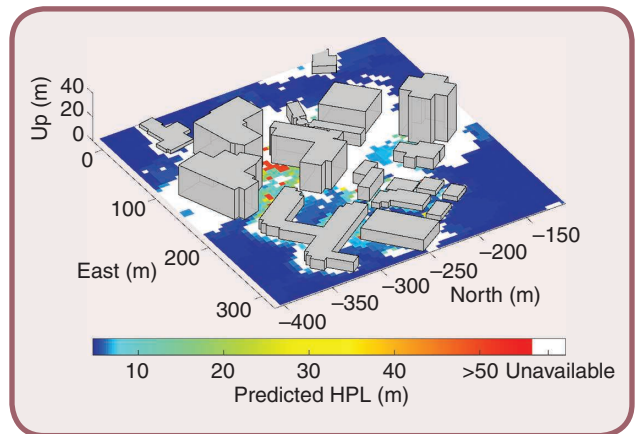


FIG 5 The conservatively predicted HPL with a 33° elevation mask at a certain time epoch. This map varies with time because of GNSS satellite motion.
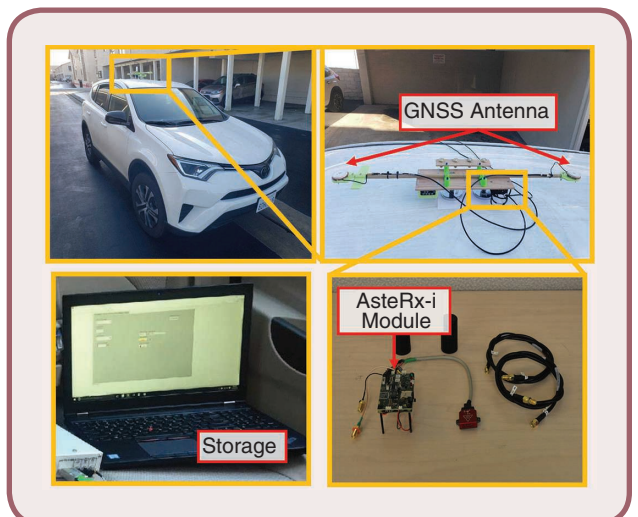


FIG 6 The experimental settings. A GNSS antenna is attached to the top of a ground vehicle. The GNSS signals are processed using a Septentrio AsteRx-i receiver module. GNSS measurements and navigation data are stored on a laptop placed inside the vehicle.

## Application Case Study: Safety-Constrained Path Planning

The predicted satellite navigation reliability map (i.e., the HPL prediction map) can be utilized by an automated vehicle for various purposes to ensure safe driving. Because the reliability of satellite navigation signals is already known through the HPL prediction map, an automated vehicle can plan a safe trajectory ahead of time. If the navigation sensors of the vehicle rely heavily on GNSS, it would be better to detour around high-HPL regions. Most automated vehicles utilize IMUs, which are calibrated using GNSS. Therefore, IMU outputs in a high-HPL region should not be relied on.

As an application case study, the path planning of an automated vehicle based on the HPL prediction map is considered. Unlike traditional strategies for path planning to minimize travel distances and times, the primary focus here is the navigation safety of an automated vehicle. Therefore, the optimization problem is formulated with safety considerations as

$$\underset{\pi \in \mathcal{P}}{\text{minimize}} \quad \sum_{p_k \in \pi} dist(p_{k-1}, p_k) \cdot HPL(p_k, t)$$

$$\text{subject to} \quad \frac{N(HPL(p_k, t) < T_{\text{HPL}})}{N_{\text{nodes}}} > T_{\text{safe}}$$

$$D_{\text{HPL unacceptable}} < D_{\text{safe}}, \qquad (5)$$

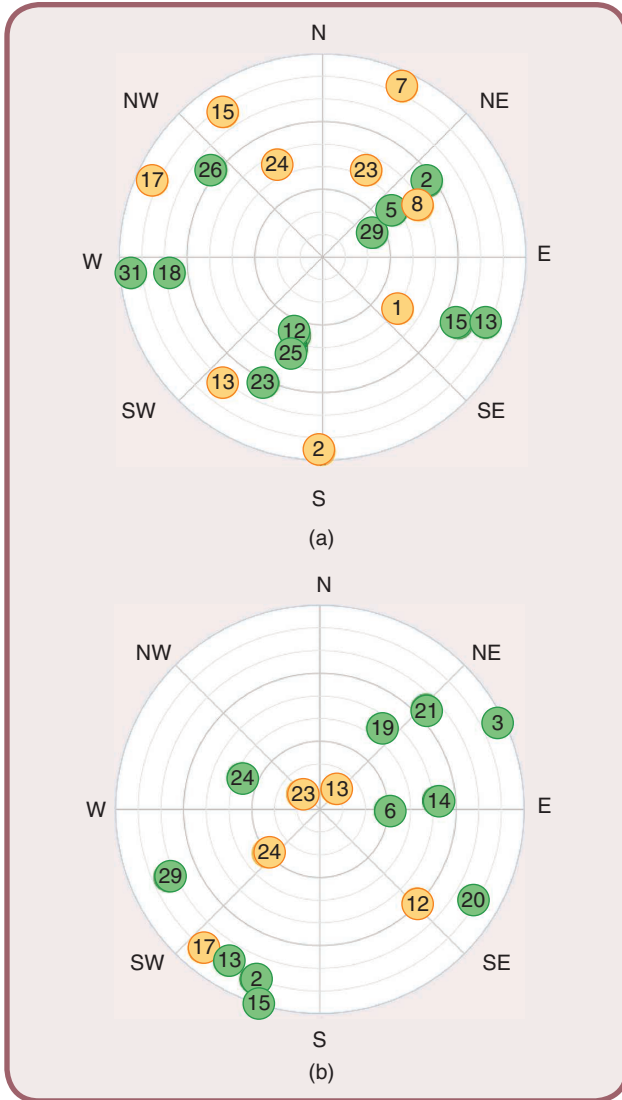where the descriptions of the symbols are given in Table 4.

FIG 7 The GPS (green) and GLONASS (yellow) constellations during the field tests in (a) Irvine and (b) Riverside.
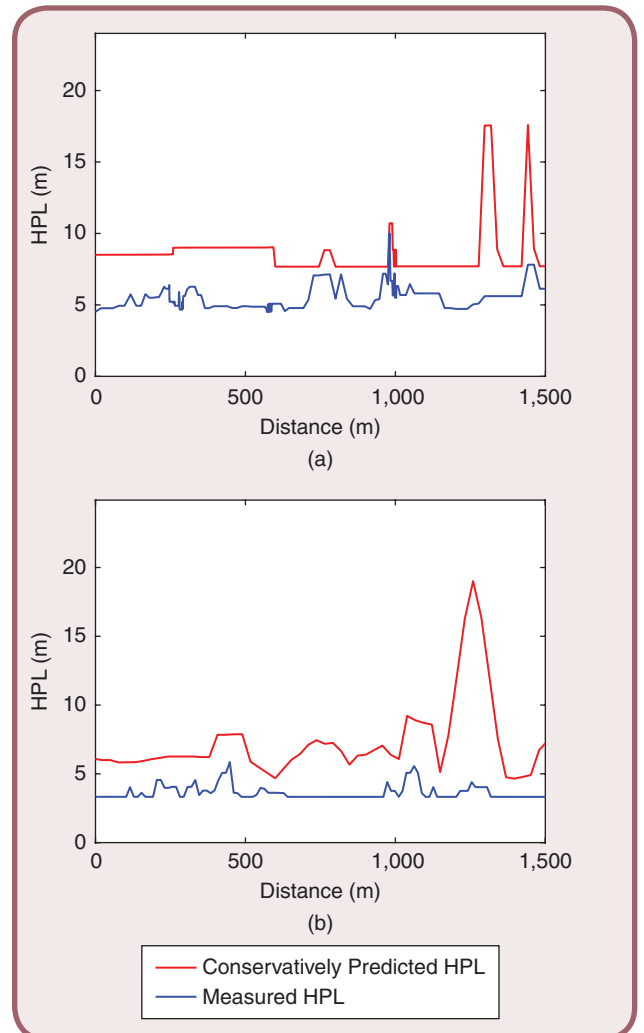
FIG 8 The urban test environment in Irvine.

FIG 9 The experimental results in (a) Irvine and (b) Riverside. Conservatively predicted HPLs overbound measured HPLs along sample paths.

The cost function in (5) aims to find an optimal path that minimizes both the travel distance and HPL along the path (recall that a smaller HPL indicates a higher satellite navigation reliability). The first constraint in (5) considers the ratio of the number of safe nodes to that of the total nodes. For example, if $T_{HPL}$ is set to 10 m and $T_{safe}$ is set to 95%, a candidate path with more than 5% of nodes having an HPL of more than 10 m will not be selected as an optimal path. The second constraint in (5) ensures the avoidance of a candidate path with continuous signal outages. The outputs from automotive-grade IMUs quickly diverge if GNSS signals are unavailable or unreliable for a certain period. Therefore, continuous signal outages are more problematic than intermittent signal outages for similar total outage durations. For example, if $D_{safe}$ is set to 150 m, a candidate path with continuous signal outages for more than a 150-m distance will not be selected as an optimal path.

Table 5 compares the optimization problem formulations of previous studies [14], [15] and the current study. Unlike the previous studies, where only travel distance and navigation reliability (i.e., the positioning error [14] and the HPL without considering measurement faults [15]) were considered, the proposed optimization problem considers GNSS unavailability and continuous signal outages, as well, to obtain a more realistic solution.

To solve the optimization problem in (5), the A* algorithm [50] was applied, which is a widely used search algorithm that can find an optimal path to a given target node. The A* algorithm was implemented as shown in Algorithm 1 to find an optimal solution to the safety-constrained path planning problem. The overall road structure of a given map, which is expressed by a graph composed of nodes and edges, is denoted by $\mathcal{P}$. Given start and target nodes, the A* algorithm finds the cheapest path [i.e., a sequence of nodes that minimizes the cost function in (5)] based on the sum of the backward cost (the cumulative cost) and forward cost (the heuristic cost). The open set, which is implemented as a priority queue that stores nodes that have been visited but whose successors have not been explored, is denoted by $O$. $p_{current}$ denotes the currently visited node, and $p_{neighbor}$ denotes a neighbor node of $p_{current}$.

For each iteration, all neighbor nodes of $p_{current}$ are stored in $O$ and the overall cost $f$ of each neighbor node is calculated. The overall cost $f$ is defined as the sum of cumulative cost $g$ and heuristic cost $h$. The Euclidean distance (i.e., the straight line distance) to the target node was used as the heuristic cost. After calculating the cost of each neighbor node, the node in $O$ with the smallest $f$ is selected as $p_{current}$ and is moved to the close set $C$. The iteration ends when the target node is reached or when the open set $O$ becomes empty. If the

target node is reached, the final optimal path $\pi$ can be found by reconstructing the nodes in $C$.

Considering the four candidate paths in Figure 10, which are between Costa Mesa, California, and Irvine, the key metrics related to the optimization problem in (5) along each candidate path are summarized in Table 6. The GPS and GLONASS pseudoranges were measured along the paths during the field tests to obtain the measured HPL. The results of this experiment are summarized as follows:

- The costs, which are the output of the cost function in (5), of paths 1, 2, 3, and 4 were 56,428, 52,137, 110,398, and 92,805, respectively. Therefore, path 2 has the minimum cost. Because path 2 satisfies all the constraints in (5), it was selected as the optimal path.
- Although the average HPLs of the four paths were similar, the ratios of safe nodes and the maximum continuous distances with unacceptable HPLs (i.e., the predicted HPL is unavailable or above $T_{HPL}$) were significantly different. In particular, in path 2, the ratio of safe nodes was 100%, and there was no section where the predicted HPL was unacceptable. This implies that an autonomous vehicle can know path 2 has better

### Table 4. The mathematical notations related to the proposed safety-constrained path planning algorithm.

| Symbol | Description |
|---|---|
| $\pi$ | Sequence of nodes between start node $p_{start}$ and target node $p_{target}$, i.e., $\pi = \{p_{start}, p_2, p_3, ..., p_{target}\}$ |
| $N_{nodes}$ | Total number of nodes along a path |
| $dist(p_{k-1}, p_k)$ | Euclidean distance between nodes $p_{k-1}$ and $p_k$ ($p_1 = p_{start}$ and $p_{N_{nodes}} = p_{target}$) |
| $HPL(p_k, t)$ | Conservatively predicted HPL at node $p_k$ and time $t$, which is given by the HPL prediction map |
| $T_{HPL}$ | Maximum allowable HPL value (i.e., the HPL threshold) |
| $N(\cdot)$ | Number of nodes satisfying the given condition |
| $T_{safe}$ | Threshold for the ratio of nodes satisfying HPL threshold $T_{HPL}$ |
| $D_{HPL\ unacceptable}$ | Continuous distance where the predicted HPL is unavailable or above $T_{HPL}$ |
| $D_{safe}$ | Threshold for $D_{HPL\ unacceptable}$ |

### Table 5. The comparison of optimization problem formulations for safety-constrained path planning.

| Method | Travel Distance | Navigation Reliability | GNSS Unavailability | Continuous GNSS Outage |
|---|---|---|---|---|
| Zhang and Hsu [14] | ✓ | ✓ | ✗ | ✗ |
| Maaref and Kassas [15] | ✓ | ✓ | ✗ | ✗ |
| Proposed | ✓ | ✓ | ✓ | ✓ |

**Algorithm 1.** The A* algorithm implementation for safety-constrained path planning.

**Data:** $\mathcal{P}, p_{start}, p_{target}, HPL, D_{safe}, T_{HPL}$
**Result:** $\pi$
$f(p_{start}) \leftarrow dist(p_{start}, p_{target})$
$D_{HPL\ unacceptable}(p_{start}) \leftarrow 0$
$safenode(p_{start}) \leftarrow 1$
$O \leftarrow p_{start}$
**while** $O$ is not empty **do**
    $p_{current} \leftarrow$ node in $O$ having smallest $f$
    $O \leftarrow O - p_{current}$
    **if** $D_{HPL\ unacceptable}(p_{current}) \geq D_{safe}$ **then**
        **continue**
    **end**
    **if** $p_{current}$ is $p_{target}$ **then**
        $\pi \leftarrow$ reconstructed path from $C$
        $N_{nodes} \leftarrow$ total number of nodes in $\pi$
        $N_{safe\ nodes} \leftarrow$ sum of $safenode$ of all nodes in $\pi$
        **if** $N_{safe\ nodes}/N_{nodes} > T_{safe}$ **then**
            **return** $\pi$
        **end**
        **continue**
    **end**
    $C \leftarrow C + p_{current}$
    **for** every neighbor of $p_{current}$ **do**
        $g(p_{neighbor}) \leftarrow dist(p_{neighbor}, p_{current}) \cdot HPL(p_{neighbor}) + g(p_{current})$
        $h(p_{neighbor}) \leftarrow dist(p_{neighbor}, p_{target})$
        $f(p_{neighbor}) \leftarrow g(p_{neighbor}) + h(p_{neighbor})$
        **if** $HPL(p_{neighbor})$ is unacceptable **then**
            $safenode(p_{neighbor}) \leftarrow 0$
            $D_{HPL\ unacceptable}(p_{neighbor}) \leftarrow$
            $D_{HPL\ unacceptable}(p_{current}) + dist(p_{neighbor}, p_{current})$
        **else**
            $safenode(p_{neighbor}) \leftarrow 1$
            $D_{HPL\ unacceptable}(p_{neighbor}) \leftarrow 0$
        **end**
        $O \leftarrow O + p_{neighbor}$
    **end**
**end**
**return** failure

GNSS signal quality than the other paths before driving by solving the optimization problem in (5) using the HPL prediction map and Algorithm 1.

- Paths 1 and 4 are also feasible solutions because they satisfied all the constraints of (5). However, neither path 1 nor path 4 is an optimal solution according to the proposed cost function that considers both travel distances and predicted HPLs.
- Path 3 is not a feasible solution because it violated the second constraint that requires $D_{HPL\ unacceptable}$ to be less than $D_{safe}$, which was set to 150 m. The proposed optimization problem successfully screened a path with continuous GNSS signal outages that could potentially threaten the vehicle's driving safety.
- In all cases, the conservatively predicted HPL bounded the measured HPL 100% of the time.

## Conclusion

The reliability of GNSS signals is crucial to ensure driving safety because various navigation sensors of automated vehicles rely on GNSS signals. This article considered the HPL obtained by the ARAIM algorithm as a metric to measure navigation reliability at a given location and time on urban roads. Due to the uncertainty of nearby dynamic objects and the limited accuracy of 3D urban digital maps, a method to conservatively predict the HPL was proposed and validated experimentally. The pseudorange biases and presence of signal reflections and blockages, which are necessary to predict the HPL in urban environments, were simulated by ray-tracing with 3D maps. The generated HPL prediction map can serve as useful road information for various navigation applications. As a case study, the HPL prediction map was applied for the safety-constrained path planning of an automated ground vehicle. Unlike previous studies, the proposed optimization problem considered the unavailability of GNSS signals and continuous GNSS signal



**FIG 10** The four candidate paths between Costa Mesa and Irvine. GNSS signals along the paths were collected during four consecutive days.

| Path | Travel Distance (m) | Average Predicted HPL (m) | Average Measured HPL (m) | Ratio of Safe Nodes (%) | Maximum Continuous Distance With Unacceptable HPL (m) |
|------|------|------|------|------|------|
| Path 1 | 9,746 | 6.49 | 5.57 | 98.5 | 131.90 |
| Path 2 | 9,631 | 7.91 | 5.60 | 100 | 0 |
| Path 3 | 14,244 | 7.67 | 5.52 | 97.2 | 208.72 |
| Path 4 | 10,629 | 8.50 | 5.64 | 97.1 | 103.95 |

Table 6. The comparison of key optimization metrics along four candidate paths.

outages that occur in urban environments. A specific implementation of the A* algorithm to find an optimal path was also suggested and demonstrated.

## Acknowledgments

## About the Authors

*Halim Lee* (halim.lee@yonsei.ac.kr) earned her B.S. degree in integrated technology from Yonsei University, Incheon, 21983, Korea, where she is a Ph.D. student in the School of Integrated Technology. Her research interests include motion planning, integrity monitoring, and opportunistic navigation.

*Jiwon Seo* (jiwon.seo@yonsei.ac.kr) earned his Ph.D. degree in aeronautics and astronautics in 2010 from Stanford University. He is an associate professor in the School of Integrated Technology, Yonsei University, Incheon, 21983, Korea. His research interests include global navigation satellite systems and complementary positioning, navigation, and timing systems. He is a member of the International Advisory Council of the Resilient Navigation and Timing Foundation and a member of several advisory committees of the Ministry of Oceans and Fisheries and the Ministry of Land, Infrastructure, and Transport, Korea. He is a Member of IEEE.

*Zaher (Zak) M. Kassas* (zkassas@ieee.org) earned his Ph.D. degree in electrical and computer engineering from the University of Texas at Austin. He is a professor of electrical and computer engineering at The Ohio State University, Columbus, Ohio, 43210, USA, and the director of the Autonomous Systems Perception, Intelligence, and Navigation Laboratory. He is also the director of the U.S. Department of Transportation Center for Automated Vehicle Research With Multimodal AssurEd Navigation (CARMEN). His research interests include cyberphysical systems, estimation theory, navigation systems, autonomous vehicles, and intelligent transportation systems. He is a senior editor of *IEEE Transactions on Intelligent Vehicles* and an associate editor of the *Transactions on Aerospace and Electronic Systems* and *IEEE Transactions on Intelligent Transportation Systems*. He is a Senior Member of IEEE.

## References

[1] J. Kim, J.-W. Kwon, and J. Seo, "Multi-UAV-based stereo vision system without GPS for ground obstacle mapping to assist path planning of UGV," *Electron. Lett.*, vol. 50, no. 20, pp. 1431–1432, 2014, doi: 10.1049/el.2014.2227.
[2] Y. Li, Z. Hu, Y. Cai, H. Wu, Z. Li, and M. Sotelo, "Visual map-based localization for intelligent vehicles from multi-view site matching," *IEEE Trans. Intell. Transp. Syst.*, vol. 22, no. 2, pp. 1068–1079, 2021, doi: 10.1109/TITS.2019.2962183.
[3] Y. Shin, S. Lee, and J. Seo, "Autonomous safe landing-area determination for rotorcraft UAVs using multiple IR-UWB radars," *Aerosp. Sci. Technol.*, vol. 69, pp. 617–624, Oct. 2017, doi: 10.1016/j.ast.2017.07.018.
[4] Z. Feng, M. Li, M. Stolz, M. Kunert, and W. Wiesbeck, "Lane detection with a high-resolution automotive radar by introducing a new type of road marking," *IEEE Trans. Intell. Transp. Syst.*, vol. 20, no. 7, pp. 2430–2447, 2019, doi: 10.1109/TITS.2018.2866079.
[5] A. Joshi and M. James, "Generation of accurate lane-level maps from coarse prior maps and lidar," *IEEE Intell. Transp. Syst. Mag.*, vol. 7, no. 1, pp. 19–29, 2015, doi: 10.1109/MITS.2014.2364081.
[6] C. Peng and Y. Zhenglin, "Modeling analysis for positioning error of mobile lidar based on multi-body system kinematics," *Intell.*

*Autom. Soft Comput.*, vol. 25, no. 4, pp. 827–834, 2019, doi: 10.31209/2019.100000086.

[7] J. Rhee and J. Seo, "Low-cost curb detection and localization system using multiple ultrasonic sensors," *Sensors*, vol. 19, no. 6, pp. 1389–1410, 2019, doi: 10.3390/s19061389.

[8] J. Wang, X. Qiu, and Y. Tu, "An improved MDS-MAP localization algorithm based on weighted clustering and heuristic merging for anisotropic wireless networks with energy holes," *Comput., Mater. Continua*, vol. 60, no. 1, pp. 227–244, 2019, doi: 10.32604/cmc.2019.05281.

[9] J. Wang, L. Cheng, Y. Tu, and S. Gu, "A novel localization approach for irregular wireless sensor networks based on anchor segmentation," *IEEE Sensors J.*, vol. 22, no. 7, pp. 7267–7276, 2022, doi: 10.1109/JSEN.2022.3145826.

[10] M. Montemerlo *et al.*, "Junior: The Stanford entry in the urban challenge," *J. Filed Robot.*, vol. 25, no. 9, pp. 569–597, 2008, doi: 10.1002/rob.20258.

[11] M. Atia *et al.*, "A low-cost lane-determination system using GNSS/IMU fusion and HMM-based multistage map matching," *IEEE Trans. Intell. Transp. Syst.*, vol. 18, no. 11, pp. 3027–3037, Nov. 2017, doi: 10.1109/TITS.2017.2672541.

[12] Z. Kassas, M. Maaref, J. Morales, J. Khalife, and K. Shamaei, "Robust vehicular localization and map matching in urban environments through IMU, GNSS, and cellular signals," *IEEE Intell. Transp. Syst. Mag.*, vol. 12, no. 3, pp. 36–52, Jun. 2020, doi: 10.1109/MITS.2020.2994110.

[13] A. Shetty and G. Gao, "Predicting state uncertainty bounds using nonlinear stochastic reachability analysis for urban GNSS-based UAS navigation," *IEEE Trans. Intell. Transp. Syst.*, vol. 22, no. 9, pp. 5952–5961, 2021, doi: 10.1109/TITS.2020.3040517.

[14] G. Zhang and L. Hsu, "A new path planning algorithm using a GNSS localization error map for UAVs in an urban area," *J. Intell. Robot. Syst.*, vol. 94, no. 1, pp. 219–235, 2019, doi: 10.1007/s10846-018-0894-5.

[15] M. Maaref and Z. Kassas, "Optimal GPS integrity-constrained path planning for ground vehicles," in *Proc. IEEE/ION Position, Location, Navig. Symp.*, 2020, pp. 655–660, doi: 10.1109/PLANS46316.2020.9109898.

[16] H. Lee, J. Seo, and Z. Kassas, "Integrity-based path planning strategy for urban autonomous vehicular navigation using GPS and cellular signals," in *Proc. ION GNSS Conf.*, 2020, pp. 2347–2357, doi: 10.33012/2020.17589.

[17] J. Jackson, B. Davis, and D. Gebre-Egziabher, "A performance assessment of low-cost RTK GNSS receivers," in *Proc. IEEE/ION Position, Location, Navig. Symp.*, 2018, pp. 642–649, doi: 10.1109/PLANS.2018.8373438.

[18] E. Costa, "Simulation of the effects of different urban environments on GPS performance using digital elevation models and building databases," *IEEE Trans. Intell. Transp. Syst.*, vol. 12, no. 3, pp. 819–829, Sep. 2011, doi: 10.1109/TITS.2011.2122258.

[19] D. Betaille, F. Peyret, M. Ortiz, S. Miquel, and L. Fontenay, "A new modeling based on urban trenches to improve GNSS positioning quality of service in cities," *IEEE Intell. Transp. Syst. Mag.*, vol. 5, no. 3, pp. 59–70, 2013, doi: 10.1109/MITS.2013.2263460.

[20] L. Wang, P. Groves, and M. Ziebart, "GNSS shadow matching: Improving urban positioning accuracy using a 3D city model with optimized visibility scoring scheme," *Navig. J. Inst. Navig.*, vol. 60, no. 3, pp. 195–207, 2013, doi: 10.1002/navi.38.

[21] K. Strandjord, P. Axelrad, and S. Mohiuddin, "Improved urban navigation with shadow matching and specular matching," *Navig., J. Inst. Navig.*, vol. 67, no. 3, pp. 547–565, 2020, doi: 10.1002/navi.378.

[22] S. Saab and Z. Kassas, "Power matching approach for GPS coverage extension," *IEEE Trans. Intell. Transp. Syst.*, vol. 7, no. 2, pp. 156–166, 2006, doi: 10.1109/TITS.2006.874720.

[23] T. Walter, P. Enge, J. Blanch, and B. Pervan, "Worldwide vertical guidance of aircraft based on modernized GPS and new integrity augmentations," *Proc. IEEE*, vol. 96, no. 12, pp. 1918–1935, Dec. 2008, doi: 10.1109/JPROC.2008.2006099.

[24] J. Lee, Y. Morton, J. Lee, H. Moon, and J. Seo, "Monitoring and mitigation of ionospheric anomalies for GNSS-based safety critical systems," *IEEE Signal Process. Mag.*, vol. 34, no. 5, pp. 96–110, 2017, doi: 10.1109/MSP.2017.2716406.

[25] J. Seo and T. Walter, "Future dual-frequency GPS navigation system for intelligent air transportation under strong ionospheric scintillation," *IEEE Trans. Intell. Transp. Syst.*, vol. 15, no. 5, pp. 2224–2236, 2014, doi: 10.1109/TITS.2014.2311590.

[26] A. Sun *et al.*, "Markov chain-based stochastic modeling of deep signal fading: Availability assessment of dual-frequency GNSS-based aviation under ionospheric scintillation," *Space Weather*, vol. 19, no. 9, pp. 1–19, Sep. 2021, doi: 10.1029/2020SW002655.

[27] H. Lee, S. Pullen, J. Lee, B. Park, M. Yoon, and J. Seo, "Optimal parameter inflation to enhance the availability of single-frequency GBAS for intelligent air transportation," *IEEE Trans. Intell. Transp. Syst.*, early access, 2022, doi: 10.1109/TITS.2022.3157138.

[28] K. Park and J. Seo, "Single-antenna-based GPS antijamming method exploiting polarization diversity," *IEEE Trans. Aerosp. Electron. Syst.*, vol. 57, no. 2, pp. 919–934, 2021, doi: 10.1109/TAES.2020.3034025.

[29] W. Kim, P.-W. Son, S. Park, S. Park, and J. Seo, "First demonstration of the Korean eLoran accuracy in a narrow waterway using improved ASF maps," *IEEE Trans. Aerosp. Electron. Syst.*, vol. 58, no. 2, pp. 1492–1496, Apr. 2022, doi: 10.1109/TAES.2021.3114272.

[30] J. Lesouple, T. Robert, M. Sahmoudi, J. Tourneret, and W. Vigneau, "Multipath mitigation for GNSS positioning in an urban environment using sparse estimation," *IEEE Trans. Intell. Transp. Syst.*, vol. 20, no. 4, pp. 1316–1528, 2019, doi: 10.1109/TITS.2018.2848461.

[31] G. Zhang and L. Hsu, "Performance assessment of GNSS diffraction models in urban areas," *Navig., J. Inst. Navig.*, vol. 68, no. 2, pp. 369–389, 2021, doi: 10.1002/navi.417.

[32] S. Saab and Z. Kassas, "Map-based land vehicle navigation system with DGPS," in *Proc. IEEE Intell. Veh. Symp.*, vol. 1, pp. 209–214, Jun. 2002, doi: 10.1109/IVS.2002.1187953.

[33] J. Bresler, P. Reisdorf, M. Obst, and G. Wanielik, "GNSS positioning in non-line-of-sight context: A survey," in *Proc. 19th IEEE Int. Conf. Intell. Transp. Syst.*, 2016, pp. 1147–1154, doi: 10.1109/ITSC.2016.7795701.

[34] P. Misra and P. Enge, *Global Positioning System: Signals, Measurements, and Performance*, 2nd ed. Lincoln, MA, USA: Ganga-Jamuna Press, 2010.

[35] J. Sleewaegen and F. Boon, "Mitigating short delay multipath: A promising new technique," in *Proc. ION Int. Tech. Meeting Conf.*, 2010, pp. 204–213.

[36] J. Blanch, A. Ene, T. Walter, and P. Enge, "An optimized multiple hypothesis RAIM algorithm for vertical guidance," in *Proc. ION GNSS Conf.*, 2007, pp. 2924–2933.

[37] J. Lee, J. Seo, Y. Park, S. Pullen, and P. Enge, "Ionospheric threat mitigation by geometry screening in ground-based augmentation systems," *J. Aircr.*, vol. 48, no. 4, pp. 1422–1433, 2011, doi: 10.2514/1.C031509.

[38] J. Seo, J. Lee, S. Pullen, P. Enge, and S. Close, "Targeted parameter inflation within ground-based augmentation systems to minimize anomalous ionospheric impact," *J. Aircr.*, vol. 49, no. 2, pp. 587–599, 2012, doi: 10.2514/1.C031601.

[39] J. Lee, S. Pullen, S. Datta-Barua, and J. Lee, "Real-time ionospheric threat adaptation using a space weather prediction for GNSS-based aircraft landing systems," *IEEE Trans. Intell. Transp. Syst.*, vol. 18, no. 7, pp. 1752–1761, 2017, doi: 10.1109/TITS.2016.2627600.

[40] R. Toledo-Moreo, M. Zamora-Izquierdo, B. Ubeda-Miarro, and A. Gomez-skarmeta, "High-integrity IMM-EKF-based road vehicle navigation with low-cost GPS/SBAS/INS," *IEEE Trans. Intell. Transp. Syst.*, vol. 8, no. 3, pp. 491–511, 2007, doi: 10.1109/TITS.2007.902642.

[41] T. Walter and J. Blanch, "Improved user position monitor for WAAS," *Navig., J. Inst. Navig.*, vol. 64, no. 1, pp. 165–175, 2017, doi: 10.1002/navi.180.

[42] J. Morales, J. Khalife, and Z. Kassas, "Opportunity for accuracy," *GPS World Mag.*, vol. 27, no. 3, pp. 22–29, Mar. 2016.

[43] M. Maaref, J. Khalife, and Z. Kassas, "Aerial vehicle protection level reduction by fusing GNSS and terrestrial signals of opportunity," *IEEE Trans. Intell. Transp. Syst.*, vol. 22, no. 9, pp. 5976–5993, Sep. 2021, doi: 10.1109/TITS.2021.3095184.

[44] J. Blanch *et al.*, "Baseline advanced RAIM user algorithm and possible improvements," *IEEE Trans. Aerosp. Electron. Syst.*, vol. 51, no. 1, pp. 713–732, 2015, doi: 10.1109/TAES.2014.130739.

[45] N. Zhu, J. Marais, D. Betaille, and M. Berbineau, "GNSS position integrity in urban environments: A review of literature," *IEEE Trans. Intell. Transp. Syst.*, vol. 19, no. 9, pp. 2762–2778, 2018, doi: 10.1109/TITS.2017.2766768.

[46] N. Ziedan, "Urban positioning accuracy enhancement utilizing 3-D buildings model and accelerated ray tracing algorithm," in *Proc. ION GNSS Conf.*, Sep. 2017, pp. 3253–3268, doi: 10.33012/2017.15366.

[47] S. Zhang, S. Lo, Y. Chen, T. Walter, and P. Enge, "GNSS multipath detection in urban environment using 3D building model," in *Proc. IEEE/ION Position, Location Navig. Symp.*, 2018, pp. 1053–1058, doi: 10.1109/PLANS.2018.8373486.

[48] S. Miura, L. Hsu, F. Chen, and S. Kamijo, "GPS error correction with pseudorange evaluation using three-dimensional maps," *IEEE Trans. Intell. Transp. Syst.*, vol. 16, no. 6, pp. 3104–3115, 2015, doi: 10.1109/TITS.2015.2432122.

[49] J. Schuster and R. Luebbers, "Comparison of site-specific radio propagation path loss predictions to measurements in an urban area," in *Proc. IEEE Antennas Propag. Soc. Int. Symp.*, 1996, pp. 1210–1213, doi: 10.1109/APS.1996.549814.

[50] S. Russell and P. Norvig, *Artificial Intelligence: A Modern Approach*, 3rd ed. Hoboken, NJ, USA: Prentice Hall, 2010.

ITS